NANO · MICRO small
www.small-journal.com

Ultra-Narrow Linewidth Photo-Emitters in Polymorphic Selenium Nanoflakes

Naveed Hussain, Shehzad Ahmed, Hüseyin U. Tepe, Kai Huang, Nardin Avishan, ShiJie He, Mohsin Rafique, Umar Farooq, Talip Serkan Kasirga, Alpan Bek, Rasit Turan, Khurram Shehzad, Hui Wu,* and Zhiming Wang**

Photoluminescence (PL) in state-of-the-art 2D materials suffers from narrow spectral coverage, relatively broad linewidths, and poor room-temperature (RT) functionality. The authors report ultra-narrow linewidth photo-emitters (ULPs) across the visible to near-infrared wavelength at RT in polymorphic selenium nanoflakes (SeNFs), synthesized via a hot-pressing strategy. Photo-emitters in NIR exhibit full width at half maximum (Γ) of 330 ± 90 μeV, an order of magnitude narrower than the reported ULPs in 2D materials at 300 K, and decrease to 82 ± 70 μeV at 100 K, with coherence time (τ_c) of 21.3 ps. The capping substrate enforced spatial confinement during thermal expansion at 250 °C is believed to trigger a localized crystal symmetry breaking in SeNFs, causing a polymorphic transition from the semiconducting trigonal (t) to quasi-metallic orthorhombic (orth) phase. Fine structure splitting in orth-Se causes degeneracy in defect-associated bright excitons, resulting in ultra-sharp emission. Combined theoretical and experimental findings, an optimal biaxial compressive strain of –0.45% cm^{-1} in t-Se is uncovered, induced by the coefficient of thermal expansion mismatch at the selenium/sapphire interface, resulting in bandgap widening from 1.74 to 2.23 ± 0.1 eV. This report underpins the underlying correlation between crystal symmetry breaking induced polymorphism and RT ULPs in SeNFs, and their phase change characteristics.

1. Introduction

The crystallization kinetics of 2D elemental chalcogenides (S, Se, Te), are extremely susceptible to external perturbations (temperature, pressure, strain, etc.). These perturbations may embed in them a fundamentally irreversible crystal disorder, nucleation, and reordering, resulting in a polymorphic phase transition: having two or more stable yet co-existing crystalline phases.[1–4] This disorder also provides optically sensitive point defects at the nucleation site, which act as a by-product and a facilitator of polymorphic transition.[5,6] The underlying mechanism stems from their relatively small electronegativity, inducing a tradeoff between ionic and covalent bonding, leading to the polymorphs possessing bonding configurations with a minuscule energy difference.[7]

Hot-pressing offers a unique strategy in which agglomerates of micro/nano-particles (NPs) are self-assembled into high-quality ultrathin 2D flakes by temperature-assisted

N. Hussain, S. He, Z. Wang
Institute of Fundamental and Frontier Sciences
University of Electronic Science and Technology of China
Chengdu, Sichuan 610054, China
E-mail: zhmwang@uestc.edu.cn

N. Hussain, A. Bek, R. Turan, K. Shehzad
Department of Physics
Middle East Technical University
Ankara 06800, Turkey
E-mail: khurrams@metu.edu.tr

N. Hussain
Department of Electrical Engineering and Computer Science
University of California Irvine
Irvine, CA 92697, USA
E-mail: huiwu@tsinghua.edu.cn

N. Hussain, H. Wu
State Key Laboratory of New Ceramics and Fine Processing
School of Materials Science and Engineering
Tsinghua University
Beijing 100084, China

The ORCID identification number(s) for the author(s) of this article can be found under https://doi.org/10.1002/smll.202204302.

S. Ahmed
State Key Laboratory for Mechanical Behavior of Materials
Xi'an Jiaotong University
Xi'an 710049, China

A. Bek, R. Turan
The Center for Solar Energy Research and Applications (ODTÜ-GÜNAM)
Ankara 06800, Turkey

H. U. Tepe, N. Avishan, A. Bek
Micro and Nano-Technology Program
School of Natural and Applied Sciences
Middle East Technical University
Ankara 06800, Turkey

K. Huang
State Key Laboratory of Information Photonics and Optical Communications & School of Science
Beijing University of Posts and Telecommunications
Beijing 100876, China

M. Rafique
Division of Quantum State of Matter
Beijing Academy of Quantum Information Sciences
Beijing 100193, China

DOI: 10.1002/smll.202204302

mechanical squashing (≈1 GPa, 250 °C) between the two substrates.[8,9] This self-assembly of NPs into thin flakes under high pressure causes the core of these flakes to experience reduced spatial degrees of freedom in all 3D (both the in-plane and out-of-plane), while their edges experience the same in only one (out-of-plane) dimension. It thus offers a decrease in entropy per unit volume, triggering a center-originated crystal symmetry breaking. This induces a crystal disorder at the nucleation site, leading to a phase transition.[5] Rich density of localized defects (at the nucleation site); a trademark feature associated with phase transition, may act as traps that host bound excitons, culminating in ultra-narrow linewidth photo-emitters (ULPs) with high color purity lasing.[10]

Because of ULPs, there has been a tremendously growing interest in 2D materials due to their compatibility with CMOS technology and flexible optoelectronics, enabling their applications from nano-lasers to quantum computing, information processing, and atomically thin displays.[11,12] ULPs are typically characterized by the full width at half maximum (Γ) of their photoluminescence (PL) peak; the lower the Γ, the higher the color purity.[13]

So far, scientists have developed material systems exhibiting ULPs in quantum dots (Γ = 21, 6.5 meV),[14,15] carbon nanotubes (Γ < 6, 13 meV),[16,17] semiconductor nanocrystals (Γ = 12, 72 meV),[18,19] and 2D materials (Γ = 1.7–9 meV).[1,20–24] ULPs in 2D materials, however, constitute an ideal platform for strong light-matter interactions due to i) their large surface-volume ratio, which reduces the total internal reflection and diffraction losses,[25] and ii) robust control and modulation in ULPs via strain and defects.[26] For quantum information processing technologies in particular, achieving absolute color purity at RT is crucial: ULPs must be distinguishable and thereby, their Γ must be in μeV range.[27] Unfortunately, cutting edge 2D materials, such as transition metal dichalcogenides (TMDCs), either exhibit Γ in meV range or require low temperatures (<150 K),[20,28] putting practical applications largely out of reach.[29,30]

In this work, using the hot-pressing method, we fabricate ultrathin selenium nanoflakes (SeNFs) that undergo a process-induced polymorphic phase transition. Combined experimental and theoretical findings reveal the coexistence of stable quasi-metallic orthorhombic selenium (*orth*-Se) (the core) and native semiconducting trigonal selenium (*t*-Se) (at edges) phases in a single Se flake. In *orth*-Se, crystal symmetry breaking and disordering introduce higher defects densities (vacancies and interstitials), which serve as a hotspot for localized and bright exciton traps. This results in ULPs across visible to thenear-infrared (NIR), with Γ = 330 ± 90 μeV at room-temperature (RT) in NIR region, which is comparable to ULPs in state-of-the-art quantum dots. The Γ further decreases to 82 ± 70 μeV with decrease in temperature to 100 K. Meanwhile, owing to the coefficient of thermal expansion (CTE) mismatch between substrate and SeNFs, *t*-Se experiences a compressive strain-induced bandgap widening (1.74 to 2.23 eV). Our findings provide a key insight into the fundamental correlation between polymorphism and RT ULPs in SeNF and broaden the current portfolio of phase change materials (PCMs).

2. Results

2.1. Fabrication and Structural Characterizations of Polymorphic SeNFs

A typical hot-pressing technique is presented in **Figure 1**a. This technique involves thermally assisted squashing of small agglomerates, comprising of selenium nanoparticles (SeNPs) directly onto c-cut sapphire (Al_2O_3) substrates, and processing them into ultrathin 2D selenium nanoflakes (SeNFs). A detailed fabrication process has been illustrated in Text S1, Supporting Information. Trigonal selenium is typically a 1D van der Waals (vdW) layered material composed of a chiral chain-like crystal lattice of distinct vdW bonded helical chains of Se atoms spiraling along [0001] direction. Each Se atom is covalently bonded with its two nearest neighbors (atomic structure is described in Figure S1a, Supporting Information. A false color field emission scanning electron microscopy (FESEM) image of an ultrathin SeNF lying on *c*-sapphire is presented in Figure 1b. The inset shows the false color FESEM image of an agglomerate of SeNPs lying on c-sapphire substrate, before being subjected to thermal squashing via hot-pressing. The FESEM image of SeNF revealed the co-existence of two distinct phases, phase I and phase II, which are separated by a dramatic textural difference (enclosed in a yellow dotted boundary). Monoelemental chalcogenides such as selenium (Se), tellurium (Te), and sulfur (S) are claimed to have the tendency to undergo polymorphic phase transition because of their extreme vulnerability toward external stimuli such as pressure, temperature, strain, etc.[31] The recent discovery of polymorphism in 2D tellurium flakes synthesized by physical vapor deposition (PVD) fortifies such claims.[32] During the hot-pressing, where agglomerates of SeNPs are self-assembled to ultrathin SeNFs, the top substrate enforces a dimensionally constrained thermal expansion in either one or both of the in-plane and out-of-plane directions. This may trigger, within the flake, a localized structural disorder that originates from a nucleation site. This causes an internal stress buildup at the interphase boundaries between the ordered and disordered structure, leading toward polymorphic phase transition.[33] Polymorphism in 2D van der Waals (vdW) heterostructures as a result of out-of-plane confinement is the exact analogy of this phenomenon.[7] In hot-press synthesis, the top substrate plays a role akin to the top layer in a vdW heterostructure, but with an added vertical

U. Farooq
Department of Physics
University of Science and Technology of China
Hefei, Anhui 230026, China
T. S. Kasirga
Institute of Materials Science and Nanotechnology
Bilkent University UNAM
Ankara 06800, Turkey
K. Shehzad
Colleges of ISEE and Microelectronics
ZJU-Hangzhou Global Scientific and Technological Innovation Center
ZJU-UIUC Institute
State Key Labs of Silicon Materials and Modern Optical Instruments
Zhejiang University
Hangzhou 310058, China

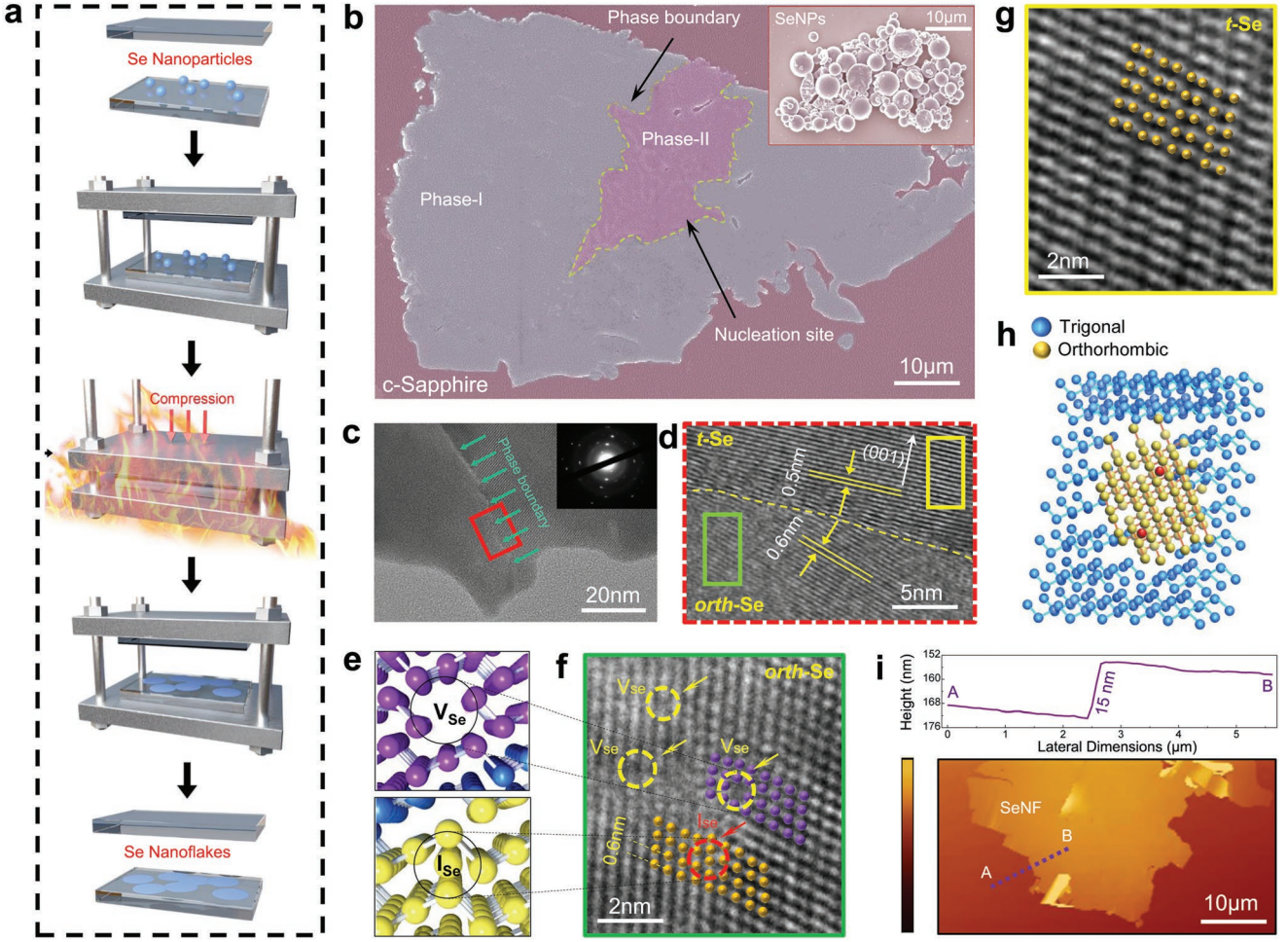

Figure 1. Hot-pressing strategy and electron microscopy characterizations of SeNFs. a) A schematic illustration of the proposed hot-pressing method used to thermally squash agglomerates of SeNPs into ultrathin SeNFs. b) False color FESEM image of a SeNF lying on c-sapphire, where a striking phase contrast reveals the co-existence of a multiphase selenium, separated by a phase boundary. The inset is the false color FESEM image of an agglomerate of SeNPs before being subjected to hot-pressing. c) Transmission electron microscopy (TEM) image showing the evidence of polymorphic phase transition within a single SeNF. The inset shows the SAED pattern, which exhibits polycrystalline nature of SeNFs. d) HRTEM image acquired from the area highlighted by a red box in Figure 1c shows two distinct and slightly misoriented crystal structures. Based on the lattice spacing measurements, the two phases can be indexed as trigonal selenium (*t*-Se) and orthorhombic selenium (*orth*-Se). e) Atomic model description of the type of defects, which mainly consist of self-interstitials (I_{Se}) and vacancies (V_{se}), respectively. f) Highly magnified HRTEM image acquired from *orth*-Se part of the SeNF (green rectangle) in Figure 1d, showing rich defect density. g) Highly magnified HRTEM image acquired from *t*-Se part of SeNF (yellow rectangle) in Figure 1d, exhibiting robust defect-free crystal lattice. h) A model constructed based on comprehensive microscopy studies, where a center-originated *orth*-Se (the yellow atomic cluster) is surrounded by *t*-Se (blue atoms). The vacancies and interstitials (red atoms) can be observed in *orth*-Se. i) An AFM image of a 15 nm thick SeNF and the corresponding height profile acquired along the purple dotted trace line.

pressure, causing thermally induced crystal symmetry breaking and triggering the first-order phase transition in SeNFs.

Classical solid-to-solid phase transitions are strictly governed by the concept of latent heat L, which is given by $L = T\Delta S$. Here, T is the transition temperature and ΔS is the difference in entropy between the two phases. Reduced dimensionality in SeNFs reduces the entropy differential ΔS significantly, lowering the required energy required to trigger phase transition. The latent heat L, during the hot-pressing, is supplied by the top and bottom substrates. Nevertheless, the total external energy provided by the hot-press in order to achieve structural phase transition in SeNFs is determined by the fundamental thermodynamic relation $dU = TdS + \sum_i Y_i dX_i$, where Y_i represents a generalized force, which in our case is P × A (pressure × area) and X_i represents the thickness reduction of flakes.[34]

To gain an in-depth insight into our hypothesis, we have performed transmission electron microscopy (TEM) investigations. A TEM image of a SeNF (Figure 1c) has revealed a distinct phase boundary, separating the two phases within a single flake. The SAED pattern acquired from the area marked (red box) in the inset of Figure 1c exhibits strong diffraction spots, indicating multi-crystal SeNFs with high crystallinity. To confirm whether the appeared line separations in Figure 1c are indeed a phase boundary, we have acquired a highly magnified HRTEM image (Figure 1d) from the area highlighted in the red box. We observed an abrupt boundary separating two distinct phases with modest crystallographic disorientation and varying crystal

lattice spacing. This denotes the presence of two structural phases, one robust and the other disordered. The ordered phase is discovered to be trigonal selenium (t-Se) with a lattice spacing of 5 Å perpendicular to the (001) plane after measuring lattice fringe spacing.[35] However, the disordered phase is revealed to be orthorhombic selenium (*orth*-Se) with a lattice spacing of 6 Å.[36] Figure 1f shows the high magnification HRTEM image acquired from the green rectangular area in Figure 1d, revealing a rich point defect density consisting of vacancies (V_{se}) and self-interstitials (I_{se}). Figure 1e presents constructed models describing V_{se} in purple, while I_{se} with yellow atoms. This geometrical construction of native point defects such as V_{se} and I_{se} exhibits a rich defect density and endorses crystal symmetry breaking in the *orth*-Se. It appears to be a foregone conclusion, as locations with higher native point defect density serve as nucleation hotspots, eventually leading to phase transition.[37] However, Figure 1g shows a nearly flawless crystal lattice of *t*-Se (derived from the yellow rectangle in Figure 1d), indicating a robust structure with extremely low defect density. Based on our extensive electron microscopy observations, it is confirmed that SeNFs, during their fabrication, undergo a process-induced polymorphic transition, which has been described with the help of an atomic model (Figure 1h). We further performed X-ray diffraction (XRD) analyzes to confirm the phase transition (Figure S2, Supporting Information). Comparative XRD (2θ) scans of bulk SeNPs and as-prepared SeNFs (on sapphire) revealed clearly distinctive diffraction patterns (Figure S2a, Supporting Information). The signal from SeNFs has been amplified by a factor of five, and confirms the signature of both the trigonal and orthorhombic phases (peaks shaded in red and green). To validate our results, we also simulated the XRD spectrum of both the *tri-Se* and *orth*-Se (Inset of Figure S2b, Supporting Information). A magnified 2θ scan of SeNFs reveals diffraction peaks at 29.5° (101), 43.6° (102), and 46.3° (111) that are assigned to the trigonal phase (JCPDS 06–0326), while the peaks at 28° (012) and 39.7° (102) have been assigned to the orthorhombic phase of selenium.[38,39] The results from XRD investigations were consistent with our HRTEM investigations and confirmed the existence of both phases in SeNFs. A 3D atomic model showing *t*-Se with an embedded (defects rich) *orth*-Se has been presented in Figure S3, Supporting Information. The model describes the relationship between the point defects and emergent polymorphism in hot-pressed SeNFs. Interestingly, thinner flakes (typically < 10 nm thick) synthesized via hot-pressing usually possess a small surface area and vice versa. Our HRTEM investigations revealed a comparatively uniform crystal lattice, and the absence of visible grain boundary in small area flakes. This suggested that thinner flakes with smaller lateral area did not undergo polymorphic phase transition. This could be attributed to the reduced dimensional constraints offered by the top-bottom substrates to the small area flakes.

An a tomic force microscopy (AFM) image of a hot-pressed Se NF on c-sapphire with a smooth surface is presented in Figure 1i. The thickness of 15 nm can be seen in the height profile recorded across the dotted purple line. The thickness distribution histogram of 100 thinnest SeNFs on c-sapphire exhibited a significant percentage (60–65%) of flakes in the 10 to 25 nm thickness range, according to the AFM data (Figure S4, Supporting Information).

2.2. Bright and Ultra-Narrow Linewidth Photo-Emitters in Polymorphic SeNFs

The optical transitions of SeNFs under illumination are expected to be largely dictated by the crystal symmetry breaking driven polymorphic phase transition, which is typically positioned around the center. To that end, the full-width at half maximum (FWHM) linewidth (Γ) of a PL peak provides useful information on the materials quality, intrinsic defects, electron-phonon coupling, structural disorders, among other things.[20] We have employed steady state micro-photoluminescence (μ-PL) emission spectroscopy over a 15 nm thick SeNF using a 532 nm laser excitation wavelength. Thinner SeNFs were not considered due to the inconclusive evidence of polymorphic phase transition. **Figure 2**a shows the results of μ-PL measurements acquired at 300, 200, and 100 K. PL response comprises multicolor photo-emitters spanning across the visible to NIR spectral range and can be classified into two types, based on their Γ value, namely type-I and type-II photo-emitters. Type-I photo-emitters, which range from visible to NIR, comprised of three RT emitters X^1, X^2, and X^3 with ultra-narrow linewidths of Γ^1, Γ^2, and Γ^3, respectively. Temperature insensitive Γ^1 (yellow emitter) at about 2.23 eV originates from *t*-Se, which is attributed to the extrinsic inhomogeneous factors such as CTE mismatch induced compressive strain, resulting in bandgap widening from direct 1.78 to 2.23 eV (described in the later section), and enhanced radiative recombination due to quantum-confinement effect.[40] Furthermore, it agrees well with our theoretically calculated bandgap (2.13 ± 0.1 eV) of compressively strained *t*-Se (later section). However, temperature-sensitive X^2 and X^3 (NIR) emitters with linewidths of Γ^2, and Γ^3, centered at 1.55 and 1.16 eV, respectively, can be specifically associated with the emissions from native defect-related bound excitons that are randomly distributed along the Fermi level in *orth*-Se. The estimated coherence time (τ_c) and lengths (l_c) of type-I photo-emitters have been presented in Text S2, Supporting information. In contrast, type-II photo-emitters, namely α^1, α^2, and α^3 exhibit rather large Γ values (several meVs) (Figure S5, Supporting Information) and are tightly positioned around the shoulders of the background PL peak of the sapphire substrate at roughly 1.79 eV, and exhibit insensitivity towards temperature. The proximity of type-II photo-emitters close to the sapphire PL peak, and their robust presence in PL spectra of both the phase-transitioned and non-phase-transition SeNFs implies that they are substantially impacted by the contributions from bulk and sapphire substrate.[41] We hypothesize that dimensionally constrained thermal expansion during the fabrication of SeNF causes a localized breaking of structural symmetry , resulting in a rather disordered structure (rich in defect density), so-called *orth*-Se,[42] which is the origin of type-I photo-emitters. Furthermore, this lack of structural symmetry not only promotes polymorphism, but also causes the lifting of energy degeneracy of (defect-associated) bright exciton states,[43] allowing the coupling of two bright exciton states.[44] This triggers a fine structure splitting (FSS) between these states, presenting relatively less control over the emission characteristics of SeNFs, but an ideal platform to realize color-pure ULPs.[45] In addition, we believe that factors such as having discrete energy

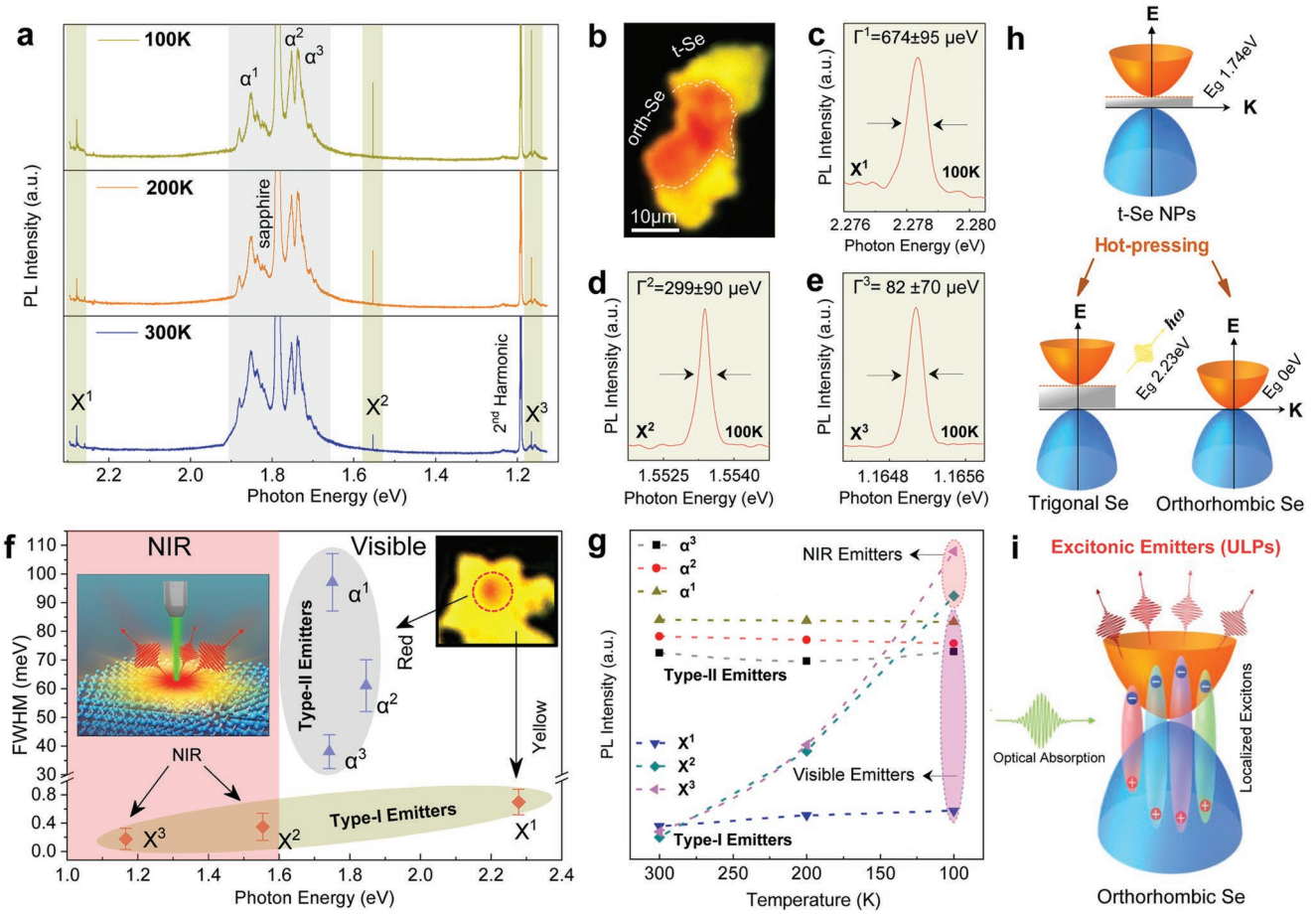

Figure 2. PL measurements of ULPs. a) PL emission spectra of polymorphic SeNFs acquired at 300, 200, and 100 °C. b) Fluorescence microscopy image of individual SeNFs showing phase-driven emission from the visible to NIR region. c–e) PL peaks of ULPs (X^1, X^2, and X^3) with their FWHM linewidths. The linewidths were acquired by performing statistical analysis using origin software, followed by subtracting the instrument broadening. f) The FWHM as a function of photoemission energy for type-I and II photo-emitters. The inset on the right shows another SeNF with type-I (yellow) and type-II yellow emissions. g) PL intensity on type-I and II photo-emitters as a function of temperature. All PL measurements were repeated five times to confirm data and its reproducibility. h) The model of electronic band structure of bulk *t-Se* before hot-pressing and both the *t*-Se and *orth*-Se after the hot-pressing. i) A schematic illustration of the existence of solitary defect-related localized excitons in *orth*-Se and their resulting ultra-narrow linewidth excitonic emission.

distribution owing to the quasi-2D nature of SeNFs, decrease in measurement temperature (≈100K), and the use of atomically flat substrate (surface roughness is presented in Figure S7, Supporting Information), have contributed synergistically to suppress the inhomogeneous broadening of the emission linewidths in SeNFs by reducing the exciton-phonon coupling strength.[46,47] To investigate flake thickness effects on photoluminescence, a PL spectrum was acquired from a 3.1 nm SeNF (Figure S8, Supporting Information). Accompanied by type-II photoemitter (α^1, α^2, α^3), the PL spectrum exhibited only yellow (out of three) emission peak (X^1) located at 2.278 eV, while other two peaks of type-I photo-emitters located in NIR region were absent. Due to its robust nature, we further performed thickness-dependent PL studies centered around X^1 peak, which exhibited no quantum confinement effects (inset of Figure S8, Supporting Information). This validates the absence of polymorphic phase transition in <10 thick SeNFs, which is also evidenced via fluorescence imaging (Figure S9, Supporting Information).

PL imaging (Figure 2b) shows strong yellow emission from the trigonal region of SeNF and suggesting a sharp transition around 2.23 eV (X^1), which is consistent with our PBE calculations and confirms the compressive strain-driven direct bandgap opening in t-Se. However, a red-NIR emission was observed from *orth*-Se, predominantly composed of defect-related excitonic ULPs in the NIR and substrate-induced type-II photo-emitters in the red spectral region. The Γ of type-I photo-emitters at 100 K have been estimated using Gaussian fitting and the results are shown in Figure 2c–e. The Γ of X^1, X^2, and X^3 photo-emitters with extremely symmetrical line-shapes is estimated to be 700 ± 95, 350 ± 90, and 178 ± 70 μeV, respectively. However, these values are pseudo-values, which need to be corrected by subtracting the instrument broadening to acquire true Γ values. Considering at least 3 data points in a resolved peak, and our instrument's spectral dispersion to be 43 μeV, the instrument broadening of spectrometer was estimated to be 43 μeV × 3 pixels = 129 μeV. Assuming instrumental broadening to obey a Gaussian distribution (w_G), the PL band

to obey a Lorentzian line (w_L), and the measured spectrum to obey a Voigt distribution (w_V), the actual linewidth (Γ) of type-I photo-emitters was estimated using the following equation:[48]

$$w_L \approx w_V - \frac{w_G^2}{0.9w_V + 0.1w_G} \quad (1)$$

After performing calculation, the actual linewidths of X^1, X^2, and X^3 photo-emitters dropped significantly down to 674 ± 95, 299 ± 90, and 82 ± 70 μeV, respectively. These are extremely small Γ values compared to the state-of-the-art quantum dots (160 μeV)[49] and h-BN at RT, demonstrating their excellent optical quality.

Energy distribution of both the type-I and II photo-emitters in relation to their FWHM is presented in Figure 2f. It is apparent that type-I photo-emitters are multicolor and distributed along a broad energy range ranging from 1.16 (NIR) to 2.23 eV (visible). However, their FWHMs are confined to a small energy range (0.178–0.7 meV), revealing their ultra-narrow linewidths. Contrarily, type-II photo-emitters exhibit FWHM spanning over large values (35 to 100 meV), while their spectral emissions are confined across a 1 eV energy range (1.75 to 1.85 eV), showing their sharp spectral bandwidth. The inset on the right shows a SeNF with small *orth*-Se responsible for all type-II and X^1 and X^2 photo-emitters, whereas, the yellow emission from flake edges is assigned to the X^3 PL peak. The inset on the left in Figure 4f is the graphic illustration of ULPs in response to the green light irradiation from a polymorphic SeNF. Figure 2g shows that the PL intensity of type-I photo-emitters, especially the ones in the NIR range, exhibit strong temperature dependency (the pink oval). Intriguingly, at T_{room}, X^3 consists of three sub-bands, resulting in a combined FWHM of 330 μeV, which merges into a singular band at 100 K, and could be attributed to the thermal broadening effect[50] (Figure S10a,b, Supporting Information). Due to this effect, the FWHM of X^3 further decreased from 387 at T_{room} to 178 μeV at 100 K. We stress that with the reduction in temperature to 100 K, the contributions from thermally activated exciton states vanish, leaving behind robust ULPs. A detailed description of how the FWHM of X^3 photo-emitter decreases with decreasing temperature from 300 to 100 K has been presented in Figure S10c, Supporting Information. The X and Y error bars were estimated by measuring each spectrum five times. Based on our PL spectroscopy investigations, the evolution in electronic band gaps after thermally squashing *t*-SeNPs to polymorphic SeNFs is illustrated in Figure 2h, revealing the semiconducting *t-Se* and quasi-metallic *orth*-Se. Figure 2i illustrates the existence of localized defect-related excitons in quasi-metallic *orth*-Se and the generation of ULPs in NIR region upon optical excitation in near-ambient conditions. The saturation behavior of PL intensity of ULPs with *the* laser excitation power (in %) is shown in Figure S11, Supporting Information.

To rule out the PL signal originating from the possible existence of selenium oxide species in SeNFs, we have investigated their chemical stoichiometry and surface composition using X-ray photoemission spectroscopy (XPS) and the results have been presented in Figure S12, Supporting Information. For SeNFs, Se $3d_{3/2}$ and Se $3d_{5/2}$ peaks are located at 55.64 eV and 54.73 eV, respectively, and arise from Se—Se bonds, indicating the metallic stoichiometry of Se. However, a rather uniform shift of ≈0.2 eV towards lower binding energies in the case of SeNFs indicates its transition towards more metallic species of quasi-2D selenium as compared with its bulk. This shift is attributed to the process-induced phase transition in 2D materials, as previously reported.[51,52] Our XPS studies (details in Text S12, Supporting Information) confirm the fabrication of highly crystalline and pure SeNFs with a hint of phase transition, without the presence of oxidation species.

2.3. Experimental and Computational Framework for Strain Estimation

We have performed comprehensive micro-Raman spectroscopy to probe structural features and phonon modes in hot-pressed SeNFs. The μ-Raman imaging of a single SeNF (tracking A_1 phonon mode) is presented in **Figure 3**a, which reveals a distinct contrast between the flake's edges and the flake's core, indicating the presence of process-induced compressive or tensile strains. The optical micrograph of the SeNF utilized for imaging can be seen in the inset. To probe phonon hardening and strain distribution, we performed Raman mapping of the same SeNF using a 100-point mesh in a region of 10×10 μm^2 (Figure 3b). In agreement with our Raman imaging results, the Raman mapping scan also reveals the presence of localized structural strains in distinctive vibrational modes. In Figure 3c, we present a comparison of Raman spectra obtained from three sites, highlighted by circles P1 (red), P2 (green), and P3 (cyan), from flake edge to core (Figure 3a). The bulk *t*-Se shows two characteristic vibrational phonon modes,[53] one of which is assigned to the transverse optical phonon mode (E_1) at 140.88 cm^{-1} while the other is a stretching phonon mode (A_1) of the 1-D chain-like structure at 233.7 cm^{-1}. As we move from point P^1 to point P^3, both the E_1 and A_1 resonant peaks demonstrate a continuous blue shift, indicating that SeNFs undergo a biaxial compressive strain (ε).

The maximum ε of −2.23% was estimated at P^1 (edge), followed by −1.51% at P^2, and −0.43% at P^3 (core). The most plausible explanation of such localized compressive strain induction in *t*-Se is the large mismatch (≈500%) between the CTE of sapphire ($\alpha_{Sapp.} = 7.1 \times 10^{-6}$ K^{-1}) and Selenium ($\alpha_{Selen.} = 37 \times 10^{-6}$ K^{-1}) during the thermal relaxation from 250 °C to RT during the hot-pressing (cited in Supporting Information). We believe that the persistent uniaxial pressure of around 1 GPa from the top substrate assisted in maintaining the non-slip condition (adhesion) between the bottom substrate and SeNF throughout their relative contraction during thermal relaxation, resulting in compressive strain propagation from the edges to the core in a Se flake.[54] A schematic representation of such a CTE mismatch and the resulting compressive strain has been shown in Figure S13a, Supporting Information. The phonon hardening in the E_1 resonant mode and the corresponding blue-shift have been presented in Figure S13c, Supporting Information, as evidence of biaxial compressive strain.

To obtain accurate information on localized phase transition, comparative μ-Raman spectra acquired from bulk *t-Se* (in blue), *orth-Se* (in green), and *t-Se* (in red) parts of a SeNF are presented

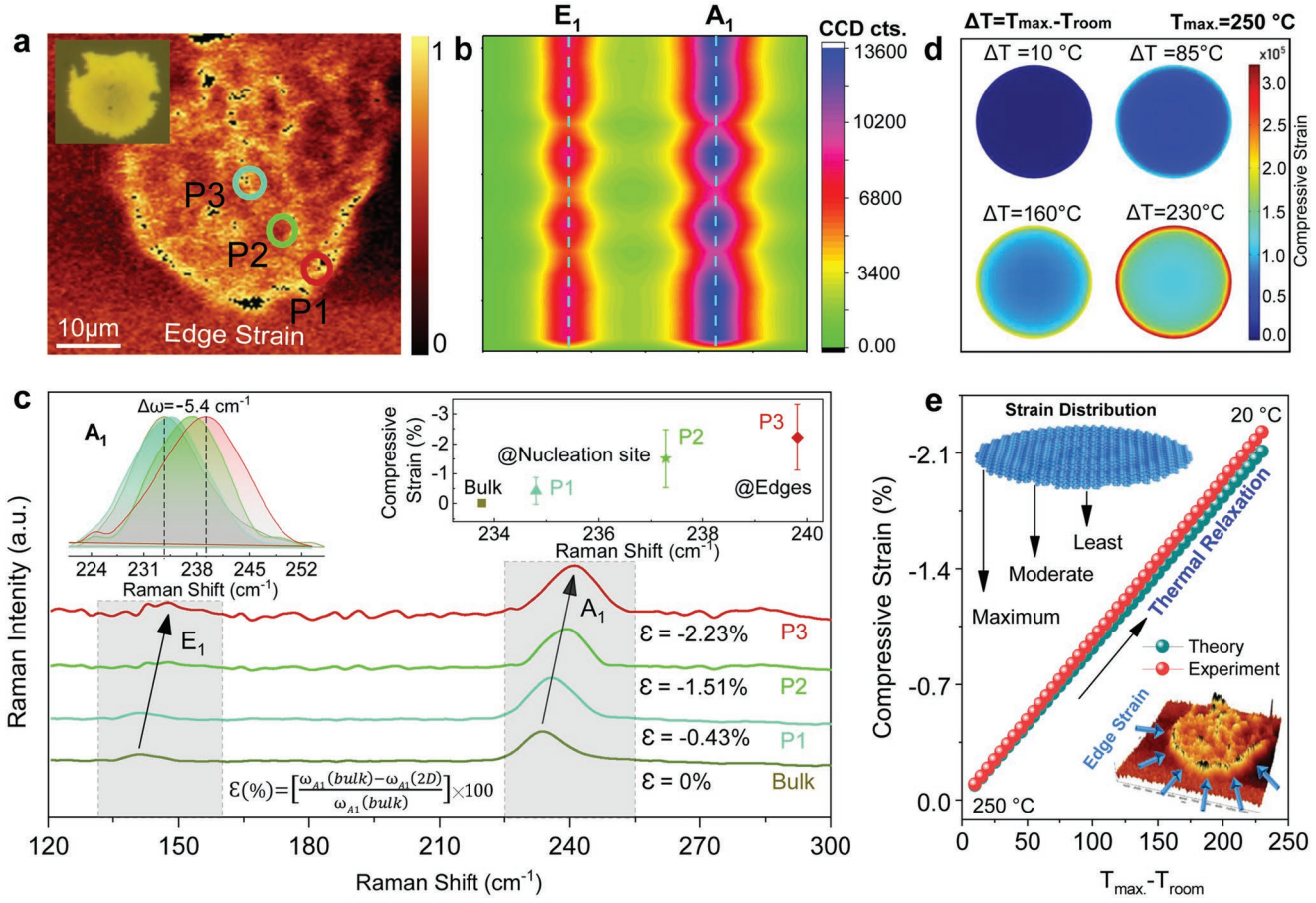

Figure 3. Experimental Raman spectroscopy studies and COMSOL modeling. a) Raman imaging of A1 mode of a SeNF, where the optical contrast hints towards the existence of strain. The inset shows an optical micrograph of the same SeNF used for Raman imaging. b) Raman map of the intensity profile of an individual SeNF confirming the presence of A_1 and E_1 phonon modes. c) Spatially distributed Raman spectra acquired from points P^1, P^2, and P^3 shown in Figure 3a in comparison with the spectra of bulk SeNPs. The inset on the top-left reveals the quantitative blue-shift in A_1 phonon mode, suggesting compressive strain and its estimation. Fluorescence microscopy image of an individual SeNF showing phase-driven photo-emission. The inset on the top-right shows the spatial distribution of compressive strain within an individual SeNF. d) COMSOL multiphysics simulation results performed for theoretical calculation of compressive strain and its incorporation mechanism at the sapphire-SeNF interface, during the thermal relaxation process in hot-pressing. e) Spectra describing both the experimentally estimated and theoretically calculated compressive strain in SeNF as a function of temperature. The inset on the top-left shows a model that demonstrates the strain distribution across the SeNFs. Whereas, the inset on the right-bottom shows 3D Raman imagining as the evidence of edge strain.

in Figure S14, Supporting Information. Selenium has space group $P3_121$ or $P3_221$ and therefore, it possesses six optical degrees of freedom. Five of them are Raman active, mainly comprised of one A_1 and two doubly degenerate E_1 modes.[55] The A_1 vibrational mode for *t*-Se appeared at 239.22 cm^{-1}, while it appears at 249.5 cm^{-1} for *orth*-Se along with a few shoulder peaks located at 187.7, 216.9, and 221.3 cm^{-1}. This is in agreement with previously reported peak values of *orth*-Se.[36] It is imperative to mention here that the principal vibrational mode A_1 for amorphous selenium has previously been reported to appear at 264 cm^{-1}, which is absent in the Raman spectra and signifies the overall high crystallinity of polymorphic SeNFs. These results emphasize the incorporation of a process-induced phase transition achieved in a single SeNF.[56] The inset on the right in Figure 3c shows the compressive strain (ε cm^{-1}), which is estimated to be as high as –0.44% cm^{-1} at P^1, while the one on the left indicates an overall Raman shift ($\Delta\omega$) of –5.4 cm^{-1} (in A_1 vibrational mode) for flake edges compared with bulk Se. The amount of perstrain in SeNFs and its type is estimated by using $\varepsilon(\%) = \frac{\omega_{A1}(\text{bulk}) - \omega_{A1}(2\text{D})}{\omega_{A1}(\text{bulk})} \times 100$, where ω_{A1}(bulk) and ω_{A1}(2D) are the A_1 Raman peak values corresponding to bulk Se and SeNFs, respectively.

For further strain analysis, we have used COMSOL Multiphysics software to simulate thermally induced stresses on ultrathin selenium flakes (details in Text S13, Supporting Information). Our simulation results presented in Figure 3d suggests that when the hot-press reaches its maximum temperature (250 °C), that is, T_{max}–T_{room} is 20 °C, the compressive strain at the c-sapphire and SeNF interface is at its least value because of their state of maximum thermal expansion. However, during the thermal relaxation to T_{room}, both the c-sapphire and SeNF contract at relatively different rates because of their CTE mismatch (see Figure S13b, Supporting Information), triggering a strain propagation from the flake edges to the core, which is consistent with our previous report on 2D germanium.[57] The

strain reaches its maximum value when the system reaches thermal equilibrium, that is, T_{max}–T_{room} is 230 °C. We present the compressive strain in SeNFs obtained from both the simulation and experimental investigations against the temperature difference (T_{max}–T_{room}) in Figure 3e. We find that theoretical and experimental compressive strains of −2.10 ± 0.1% and −2.23 ± 0.2%, respectively, are in close agreement with each other. The inset in Figure 3e at top left shows a graphical illustration of strain distribution and its mode of propagation in SeNF. The inset at bottom right is the 3D Raman image illustrating the edge strain in Se NFs. Both the computational and experimental estimation of stress and strain as a function of thermal relaxation have been presented in Figure S15, Supporting Information.

2.4. Computational Studies for Optical Contrast and E-Band Structure of Polymorphic SeNFs

First-principle calculations have been performed in order to confirm the electronic band structure of both the *t*-Se and *orth*-Se phases in relation to their PL spectroscopy results (discussed in Figure 2). All calculations are performed using the projector augmented wave method as implemented in the Vienna ab-initio simulation package (VASP),[58] coupled with a generalized gradient approximation (GGA) electron-electron interaction defined as Perdew–Burke–Ernzerhof (PBE) exchange-correlation functional.[59] We calculate their electron localization function (ELF) which is presented in **Figure 4**a.[60] Moreover, the band structure and total density of states are examined to further study the electronic properties of *t*-Se and *orth*-Se as shown in Figure 4b. Our results indicate that the valence band maxima (VBM) and the conduction band minima (CBM) of *t*-Se and *orth*-Se are located at the Γ point with a band gap of 2.13 eV which is consistence with our experimental PL spectroscopy data (previous section). Further, the total densities of states (DOSs) in the energy range −5 to 5 eV are computed. Thus, we observe that Se-p states contribute to the valence band near the Fermi energy. The results of the electron density of states (DOS) suggest that t-Se compounds are wide bandgap semiconductors. In addition, the metallic bandgap for *orth*-Se originates due to delocalized p orbitals.

For *orth*-Se and *t*-Se layers, we employed PBE simulations with van der Waals corrections, and the calculated complex dielectric functions are presented in Text S5, Supporting Information. The layered *t*-Se and *orth*-Se structure of the compounds means the optical properties are highly anisotropic. Because the fundamental motive for checking these properties is appropriateness, a more extensive examination of the predicted absorption coefficients in the visible light band (1.65 – 3.26 eV) is required (Figure 4c,d). In the low energy range, its absorption coefficient appears to be practically isotropic. For both phases, the absorption coefficient and extinction coefficient are somewhat anisotropic on ‖x and ‖y directions, as evidenced by the visually distinct curve forms in both directions.

Aside from the absorption onset shift caused by band gap variations, adjusting Se ordering results in identical optical characteristics, including absorption edges. To recapitulate, the *t*-Se has wide bandgap and its absorption properties lie in the visible range as compared to the *orth*-Se with no bandgap.

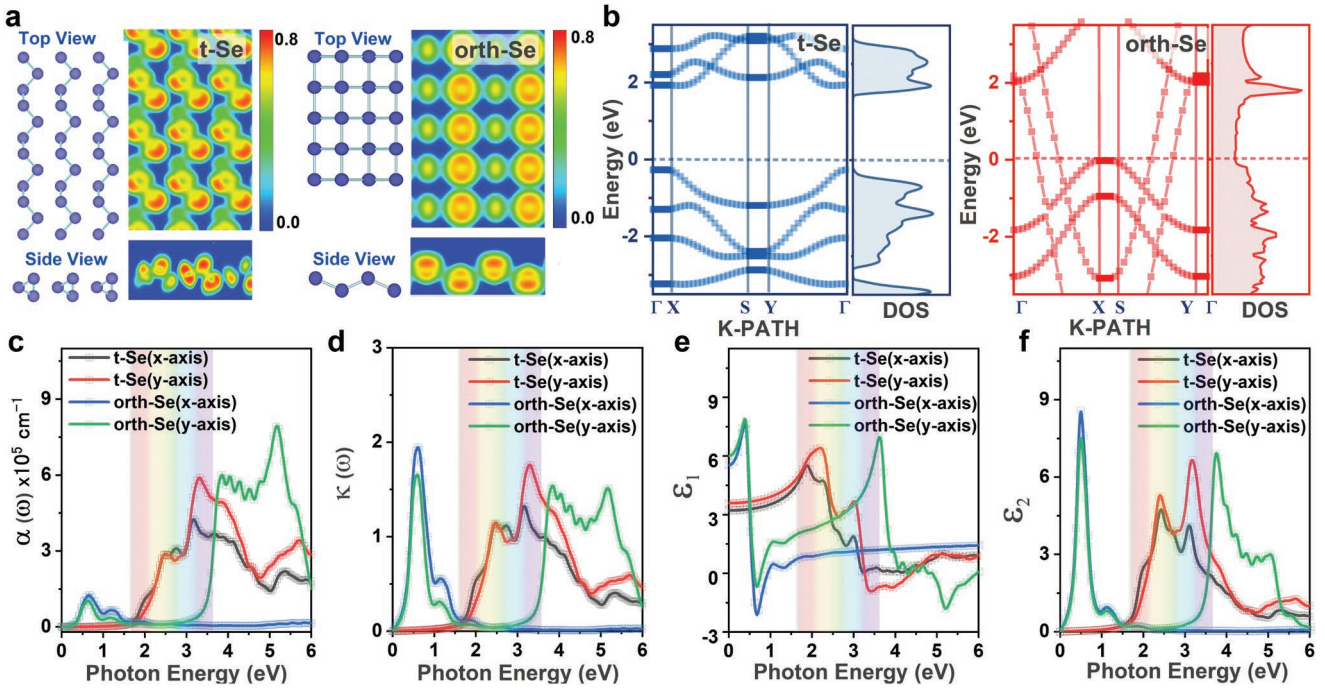

Figure 4. Computational dynamics of polymorphic phases. a) Relaxed atomic structures of 2D t-Se and *orth*-Se with respect to their ELF to understand chemical bonding from electronic structure calculations, respectively. b) Total density of state analysis mapped out from DFT/GGA calculations, and their band structures dashed line indicates Fermi level is at 0 eV. Demonstration of the calculated optical properties of quasi-2D *t*-Se and *orth*-Se along x and y direction: c) Absorption coefficient of *t*-Se and *orth*-Se, d) variation in refractive index with energy. e) Variation in the real part of the dielectric function with energy. f) Variation in the imaginary part of dielectric function with energy.

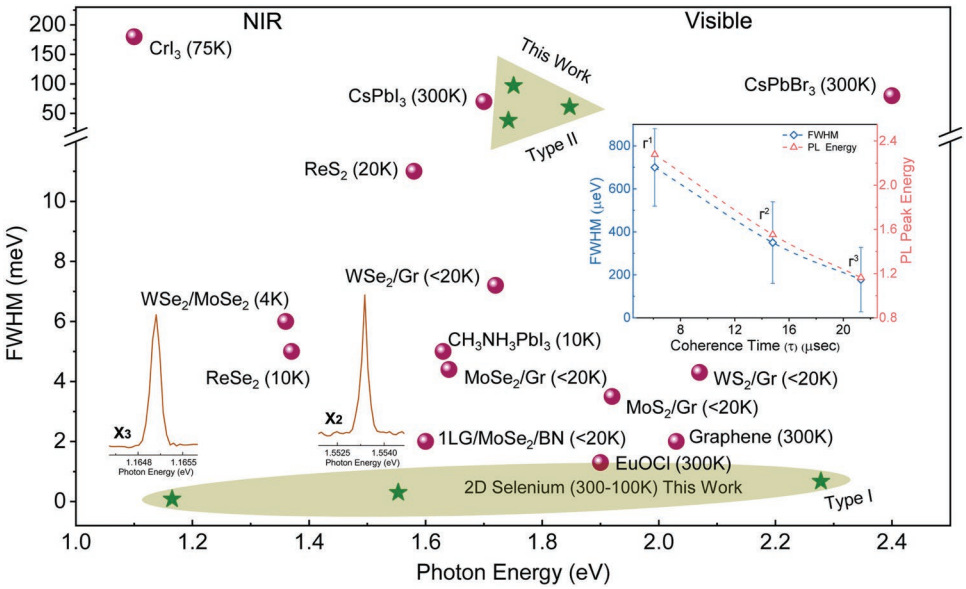

Figure 5. Previously reported PL linewidths in 2D materials. A comparison of FWHM (Γ) values of previously reported 2D materials systems (EuOCl,[1] ReS_2,[22] MoS_2,[23] $MoSe_2$,[23] WS_2,[23] WSe_2,[23] and $CsPbI_3$,[24] $CsPbBr_3$[24]) and our polymorphic SeNFs, as a function of their emission energy. Green ellipse and triangle represent linewidth (Γ) of type-I and type-II photo-emitters in SeNFs, respectively. The inset shows the coherence time (ps) of X^1, X^2, and X^3 photo-emitters and their corresponding FWHM and PL peak energy.

Furthermore, the Se compounds studied have low reflectivity and high absorptivity in the IR-Visible-UV region of the spectra. At lower energies, there is a shoulder and a relatively steep decrease below 1.6 eV at a minimum. We show both the real $\varepsilon_1(\omega)$ and the imaginary $\varepsilon_2(\omega)$ parts of the dielectric function, in their *x* and *y* directional components, in Figure 4e,f. We also observe that the imaginary portion of the dielectric function $\varepsilon_2(\omega)$ remain nearly zero-valued below the band gap for the *t*-Se and rises substantially at energies immediately above the gap for *orth*-Se Figure S16a,b, Supporting Information. These phases $\varepsilon_2(\omega)$ encompass almost the whole telecom wavelength and visible light spectrum.

Figure 5 provides a comparative overview of previous reports on the PL FWHM of ULPs in 2D materials and their vdW heterostructure assemblies. Type-I photo-emitters in SeNFs, particularly in NIR region, exhibit the narrowest linewidth, which is approximately an order of magnitude narrower than the reported PL linewidth (~1.2 meV) at RT. The inset shows the FWHM and PL peak energy of type-I photo-emitters (X^1, X^2, and X^3) as a function of coherence time (τ_c) (ps). The τ_c of the photoemissions is found to be highly sensitive to that of the FWHM, as it increases with narrowing the linewidth, and the longest obtained τ_c is 21.3 ps for X^3 photo-emitters in NIR spectral region.

3. Conclusion

In summary, we employ a facile hot-pressing strategy to thermo-mechanically squash SeNPs sandwiched between the c-sapphire substrates to fabricate ultrathin SeNFs for the first time. PL spectroscopy studies conducted over SeNFs uncover ULPs across the UV to NIR spectral region at RT. The least FWHM (Γ^3) obtained from NIR peak X^3 is 330 ± 90 μeV, which shrinks to 82 ± 70 μeV as temperature drops from 300 to 100 K, which is comparable to the narrowest linewidth reported to date at RT. The phenomenon could be attributed to the process-induced, center-originated localized polymorphic phase transition from native *t*-Se (semiconducting) to *orth*-Se (metallic) in SeNFs, driven by the space-confined thermal expansion of selenium. Disordered nucleation cites in *orth*-Se experience crystal symmetry breaking, resulting in solitary defects that operate as degenerate light exciton traps, yielding ULPs in the UV to NIR spectral region. Theoretical and computational studies confirm that *t*-Se being on the edges undergoes a compressive strain of −2.23% due to the mismatch in CTE between the sapphire and SeNFs, resulting in the bandgap widening from 1.78 to 2.23 ± 0.1 eV and a strong yellow photoemission. This work elucidates the fundamental correlation between polymorphism and RT ULPs in SeNF. Additional research such as photon correlation statistics and lifetime measurements are required to fully exploit the potential of the ULPs in SeNFs as photon sources for application in room-temperature quantum photonics.

4. Experimental Section

Materials: Commercially available Se nanoparticles with the size distribution of 300–800 nm (Sigma Aldrich, 99.99%) were used without any processing to prepare an ethanol/SeNPs (50 mL/10 mg) dispersion. Atomically flat (1 × 1 cm^2) c-cut sapphire (Al_2O_3) substrates (KYKY Technology Co. LTD) were ultrasonicated in acetone, ethanol, and distilled water. To obtain moisture-free surfaces of c-sapphire before mass-loading, the substrates were placed in a furnace maintained at 70 °C for 30 min. A commercial hot-press system (AH-4015, 200 V-20A, Japan) was used for thermo-mechanical squashing of SeNPs to fabricate ultrathin SeNFs.

Fabrication of Polymorphic SeNFs: Mass-loading was performed by drop-casting the 20 μL of the homogeneous ethanol/SeNPs dispersion onto a 1 × 1 cm^2 c-cut sapphire substrate by using a micropipette. The loaded substrate was left to dry for 30 min in an Argon-filled glove box

(MB200MOD) to avoid unnecessary exposure to moisture and dust particles. After the complete evaporation of ethanol, the c-sapphire substrate capped with large agglomerates of SeNPs of different sizes and shapes was taken out of the glovebox and was further covered by another sapphire substrate thus sandwiching the SeNPs. This sandwich (sapphire-SeNPs-sapphire) was then placed in the middle of the metal plates of the hot-press machine. During thermo-mechanical squashing, the temperature of the hot-press was raised from RT to 250 °C, while the pressure was gradually increased from the atmospheric pressure to 0.996 GPa. The sapphire-SeNPs-sapphire assembly was hot-pressed for 20 min at 250 °C before cooling (thermal relaxation) it down to RT, while maintaining a constant pressure of 0.996 GPa throughout the relaxation process. The obtained sample was studied without any post-fabrication annealing.

Theoretical Calculations: The frequency-dependent dielectric matrix was calculated within the independent-particle approximation. Local field effects and many body effects were not considered, which was proven to be adequate to quantify the optical contrast between hexagonal and orthorhombic phases of bulk and SeNFs. The frequency-dependent complex dielectric function $\varepsilon(\omega)$ where, $\varepsilon(\omega) = \varepsilon_1(\omega) + i\,\varepsilon_2(\omega)$ can be used to determine the linear optical characteristics of semiconductors, where ω is the photon frequency and $\varepsilon_1(\omega)$ and $\varepsilon_2(\omega)$ are the real and imaginary parts of the dielectric function, respectively. Within the one-electron picture, the imaginary part of the dielectric function $\varepsilon_2(\omega)$ is obtained from the following equation:

$$\varepsilon_2(\omega) = \frac{4\pi^2 e^2}{\Omega} \lim_{q\to 0} \frac{1}{q^2} \times \sum_{c,v,k} 2w_k \delta(E_c - E_v - \omega) \left|\langle c|\mathrm{e.q}|v\rangle\right|^2 \quad (2)$$

Where $\langle c|\mathbf{e.q}|v\rangle$ signifies the joint optical transition from states of the valence band (v) to the conduction band (c), e is the direction of polarization of the photon, and q is the electron momentum operator. The integration over the k's is a sum over special k-points with corresponding weighting factors w_k. The real part of the dielectric function $\varepsilon_1(\omega)$ was obtained from the imaginary part $\varepsilon_2(\omega)$ based on the usual Kramers–Kronig transformation.

$$\varepsilon_1(\omega) = 1 + \frac{2}{\pi} P \int_0^\infty \frac{\varepsilon^{(2)}_{\alpha\beta}(\omega')\omega'}{\omega^2 - \omega^2 + i\eta} \mathrm{d}\omega' \quad (3)$$

Here, P denotes the principal value and η is the complex shift parameter. The frequency-dependent linear optical spectra, for example, refractive index $\eta(\omega)$, extinction coefficient $k(\omega)$, absorption coefficient $\alpha(\omega)$, energy-loss function $L(\omega)$, and reflectivity $R(\omega)$ can be calculated from the real $\varepsilon_1(\omega)$ and the imaginary $\varepsilon_2(\omega)$ parts:

$$\varepsilon_2(\omega) = \frac{\sqrt{2}\omega}{c}\left[\sqrt{\varepsilon_1^2 + \varepsilon_2^2} - \varepsilon_1\right]^{\frac{1}{2}} \quad (4)$$

$$k(\omega) = \left[\frac{\sqrt{\varepsilon_1^2 + \varepsilon_2^2} - \varepsilon_1}{2}\right]^{\frac{1}{2}} \quad (5)$$

Material Characterizations: Morphology of SeNFs was studied by using FESEM, (MERLIN VP compact, Carl Zeiss, Germany). A multipurpose JEOL-2100 analytical electron microscope with the resolution as high as 0.19 nm, operated at 200 to 80 kV was used to perform the transmission electron microscopy (TEM), high-resolution transmission electron microscopy (HRTEM), and selected area electron diffraction (SAED) measurements. To prepare TEM samples, c-sapphire capped with hot-pressed SeNFs was immersed in ethanol and sonicated for 30 min to isolate SeNFs from sapphire into the ethanol solution. The ethanol-containing SeNFs were dropped onto the carbon-coated Cu grid by a micropipette to perform TEM/HRTEM characterizations. For scanning probe microscopy characterizations, an Asylum Research Cypher AFM (SPM, SHIMADZU Corporation, spm-9600) in tapping mode was employed to investigate surface topography and thicknesses of polymorphic SeNFs. A Raman spectrometer (LabRAM HR Evolution, HORIBA Jobin Yvon, France) with an objective lens (Nikon Plan Fluor 50 X, N.A. = 0.4) and the laser spot size of approximately 2 µm was deployed to acquire Micro-Raman spectra of polymorphic SeNFs lying a c-sapphire. XPS (Escalab, 250 Xi, Thermo Fisher Scientific, MA, USA), equipped with an A1Kα radiation source (1487.6/eV) was used to investigate the chemical composition and stoichiometry of SeNFs. The binding energy calibration was performed carefully by using C1s peak (284.8 eV) as reference value. PL measurements of SeNFs from RT to cryogenic temperatures with variable laser power ranging from 0.2–1 mW were performed by using LabRAM HR Evolution, HORIBA Jobin Yvon, France, equipped with a 532 nm Nd: YAG (Nd: $Y_3Al_5O_{12}$) laser, and a CCD detector. A portable continuous flow cryostat (ST-500-UC) with a limited temperature range (from RT to 90 K) and supplied by liquid Helium was used for low-temperature PL measurements.

Pressure Calculation: The pressure applied during hot-press for mechanically squashing SeNPs to fabricate ultrathin SeNFs was estimated by the following expression:

$$\mathrm{P} = \frac{P_0 \times \mathrm{A}_0}{a_0} = \frac{\left(55\times10^6 \mathrm{Nm}^{-2}\right)\left(3.1416\times\left(24\times10^{-3}\mathrm{m}\right)^2\right)}{\left(1\times10^{-4}\mathrm{m}^2\right)} = 0.996\ \mathrm{GPa} \cong 1\ \mathrm{GPa} \quad (6)$$

Where "P_0" is applied pressure, "A_0" is the area of the cylinder, and "a" is the area of the substrate.

Statistical Analyzes: Statistical analysis of the data including mean values and their standard deviation, and linear curve fittings were performed by using origin software. PL data has been corrected for instrument broadening, which calculated the analytical tool.

Supporting Information

Supporting Information is available from the Wiley Online Library or from the author.

Acknowledgements

This study was jointly supported by the 2232 Internatioal Fellowship for Outstanding Researchers Program of Tubitak (Project No: 118C214), National Key Research and Development Program (No. 2019YFB2203400), the National Basic Research of China (Grants 2015CB932500, 2016YFE0102200, and 2018YFB0104404), and National Natural Science Foundations of China (Grants 12150410313, 51788104, 51661135025, 51706117, 62050410351 and U1564205). [Correction added after publication 23 October 2022: The author name "Khurram Shahzad" was corrected to "Khurram Shehzad"; the affiliation of Z. Wang was corrected; the order of Figure 3 and Figure 4 was corrected (the images and captions were swapped). Correction added after publication 28 December 2022: the affiliations were updated].

Conflict of Interest

The authors declare no conflict of interest.

Author Contributions

N.H. initiated the project after consultation with H.W. N.H. synthesized and performed structural characterizations of polymorphic SeNFs. N.H. fabricated the samples for optical measurements. A.S. performed PBEE simulations to analyze electronic structure of different phases. H.T. performed COMSOL Multiphysics simulations for compressive strain estimation. N.H., N.A., T.S.K., A.B., and K.S. performed the data analysis. N.H. and A.S. wrote the manuscript with contributions from all other authors. N.H., K.S., H.W., and Z.W. supervised the project.

Data Availability Statement

The data that support the findings of this study are available from the corresponding author upon reasonable request.

Keywords

2D materials, hot-pressing, polymorphic phase-transition, selenium nanoflakes, ultra-narrow linewidth photo-emitters

Received: July 12, 2022
Revised: September 2, 2022
Published online: October 17, 2022

[1] P. Chen, Z. Li, D. Li, L. Pi, X. Liu, J. Luo, X. Zhou, T. Zhai, *Small* **2021**, *17*, 2100137.
[2] F. Peyskens, C. Chakraborty, M. Muneeb, D. Van Thourhout, D. Englund, *Nat. Commun.* **2019**, *10*, 4435.
[3] K. L. Seyler, D. Zhong, D. R. Klein, S. Gao, X. Zhang, B. Huang, E. Navarro-Moratalla, L. Yang, D. H. Cobden, M. A. McGuire, *Nat. Phys.* **2018**, *14*, 277.
[4] M. Amani, D.-H. Lien, D. Kiriya, J. Xiao, A. Azcatl, J. Noh, S. R. Madhvapathy, R. Addou, K. Santosh, M. Dubey, *Science* **2015**, *350*, 1065.
[5] D. Rhodes, S. H. Chae, R. Ribeiro-Palau, J. Hone, *Nat. Mater.* **2019**, *18*, 541.
[6] P. K. Chow, R. B. Jacobs-Gedrim, J. Gao, T.-M. Lu, B. Yu, H. Terrones, N. Koratkar, *ACS Nano* **2015**, *9*, 1520.
[7] W. Li, X. Qian, J. Li, *Nat. Rev. Mater.* **2021**, *6*, 829.
[8] N. Hussain, M. Rafique, T. Anwar, M. Murtaza, J. Liu, F. Nosheen, K. Huang, Y. Huang, J. Lang, H. Wu, *2D Mater.* **2019**, *6*, 045006.
[9] N. Hussain, T. Liang, Q. Zhang, T. Anwar, Y. Huang, J. Lang, K. Huang, H. Wu, *Small* **2017**, *13*, 1701349.
[10] L. Linhart, M. Paur, V. Smejkal, J. Burgdörfer, T. Mueller, F. Libisch, *Phys. Rev. Lett.* **2019**, *123*, 146401.
[11] W. Du, C. Li, J. Sun, H. Xu, P. Yu, A. Ren, J. Wu, Z. Wang, *Laser Photonics Rev.* **2020**, *14*, 2070066.
[12] X. Liu, M. C. Hersam, *Nat. Rev. Mater.* **2019**, *4*, 669.
[13] Q. Zhang, R. Su, X. Liu, J. Xing, T. C. Sum, Q. Xiong, *Adv. Funct. Mater.* **2016**, *26*, 6238.
[14] K. Nishi, H. Saito, S. Sugou, J.-S. Lee, *Appl. Phys. Lett.* **1999**, *74*, 1111.
[15] A. Surrente, P. Gallo, M. Felici, B. Dwir, A. Rudra, E. Kapon, *Nanotechnology* **2009**, *20*, 415205.
[16] H. Htoon, M. O'Connell, S. Doorn, V. Klimov, *Phys. Rev. Lett.* **2005**, *94*, 127403.
[17] J. Lefebvre, Y. Homma, P. Finnie, *Phys. Rev. Lett.* **2003**, *90*, 217401.
[18] I. Sychugov, A. Fucikova, F. Pevere, Z. Yang, J. G. Veinot, J. Linnros, *ACS Photonics* **2014**, *1*, 998.
[19] J. Cassidy, C. Ellison, J. Bettinger, M. Yang, P. Moroz, M. Zamkov, *Chem. Mater.* **2020**, *32*, 7524.
[20] O. A. Ajayi, J. V. Ardelean, G. D. Shepard, J. Wang, A. Antony, T. Taniguchi, K. Watanabe, T. F. Heinz, S. Strauf, X. Zhu, *2D Mater.* **2017**, *4*, 031011.
[21] F. Cadiz, E. Courtade, C. Robert, G. Wang, Y. Shen, H. Cai, T. Taniguchi, K. Watanabe, H. Carrere, D. Lagarde, *Phys. Rev. X* **2017**, *7*, 021026.
[22] X. Wang, K. Shinokita, Y. Miyauchi, N. T. Cuong, S. Okada, K. Matsuda, *Adv. Funct. Mater.* **2019**, *29*, 1905961.
[23] E. Lorchat, L. E. P. López, C. Robert, D. Lagarde, G. Froehlicher, T. Taniguchi, K. Watanabe, X. Marie, S. Berciaud, *Nat. Nanotechnol.* **2020**, *15*, 283.
[24] R. Zhang, Su, X. L. , J. Xing, T. C. Sum, Q. Xiong, *Adv. Funct. Mater* **2016**, *26*, 6238.
[25] C. Chakraborty, N. Vamivakas, D. Englund, *Nanophotonics* **2019**, *8*, 2017.
[26] A. Branny, S. Kumar, R. Proux, B. D. Gerardot, *Nat. Commun.* **2017**, *8*, 15053.
[27] A. W. Schell, H. Takashima, T. T. Tran, I. Aharonovich, S. Takeuchi, *ACS Photonics* **2017**, *4*, 761.
[28] K. Parto, S. I. Azzam, K. Banerjee, G. Moody, *Nat. Commun.* **2021**, *12*, 3585.
[29] Y. Bai, L. Zhou, J. Wang, W. Wu, L. J. McGilly, D. Halbertal, C. F. B. Lo, F. Liu, J. Ardelean, P. Rivera, *Nat. Mater.* **2020**, *19*, 1068.
[30] J.-P. So, H.-R. Kim, H. Baek, H.-C. Lee, W. Huh, Y. S. Kim, K. Watanabe, T. Taniguchi, J. Kim, C.-H. Lee, *Sci. Adv.* **2021**, *7*, eabj3176.
[31] S. Demirci, H. H. Gürel, S. Jahangirov, S. Ciraci, *Nanoscale* **2020**, *12*, 3249.
[32] A. Apte, E. Bianco, A. Krishnamoorthy, S. Yazdi, R. Rao, N. Glavin, H. Kumazoe, V. Varshney, A. Roy, F. Shimojo, *2D Mater.* **2018**, *6*, 015013.
[33] A. Pal, S. Gohil, S. Sengupta, H. Poswal, S. M. Sharma, S. Ghosh, P. Ayyub, *J. Phys.: Condens. Matter* **2015**, *27*, 415404.
[34] D. A. Rehn, Y. Li, E. Pop, E. J. Reed, *npj Comput. Mater.* **2018**, *4*, 2.
[35] X. Li, Y. Li, S. Li, W. Zhou, H. Chu, W. Chen, I. L. Li, Z. Tang, *Cryst. Growth Des.* **2005**, *5*, 911.
[36] K. Nagata, H. Tashiro, Y. Miyamoto, *Jpn. J. Appl. Phys.* **1981**, *20*, 2265.
[37] Z. Zhang, W. Liu, B. Zhang, B. Sateesh, L. Yuan, D. Zhu, P. Guan, S. J. Pennycook, J. Guo, *2D Mater.* **2021**, *8*, 025017.
[38] Z.-Y. Jiang, Z.-X. Xie, S.-Y. Xie, X.-H. Zhang, R.-B. Huang, L.-S. Zheng, *Chem. Phys. Lett.* **2003**, *368*, 425.
[39] G. Parthasarathy, W. Holzapfel, *Phys. Rev. B* **1988**, *38*, 10105.
[40] E. Piacenza, A. Presentato, B. Heyne, R. Turner, *Nanophotonics* **2020**, *9*, 3615.
[41] M. Buscema, G. A. Steele, H. S. van der Zant, A. Castellanos-Gomez, *Nano Res.* **2014**, *7*, 561.
[42] A. Rastelli, M. Stoffel, A. Malachias, T. Merdzhanova, G. Katsaros, K. Kern, T. H. Metzger, O. G. Schmidt, *Nano Lett.* **2008**, *8*, 1404.
[43] R. Trotta, E. Zallo, C. Ortix, P. Atkinson, J. D. Plumhof, J. van den Brink, A. Rastelli, O. G. Schmidt, *Phys. Rev. Lett.* **2012**, *109*, 147401.
[44] A. J. Bennett, M. A. Pooley, R. M. Stevenson, M. B. Ward, R. B. Patel, A. B. de la Giroday, N. Sköld, I. Farrer, C. A. Nicoll, D. A. Ritchie, A. J. Shields, *Nat. Phys.* **2010**, *6*, 947.
[45] C. Chakraborty, N. R. Jungwirth, G. D. Fuchs, A. N. Vamivakas, *Phys. Rev. B* **2019**, *99*, 045308.
[46] K. Leng, I. Abdelwahab, I. Verzhbitskiy, M. Telychko, L. Chu, W. Fu, X. Chi, N. Guo, Z. Chen, Z. Chen, *Nat. Mater.* **2018**, *17*, 908.
[47] M. D. Tessier, C. Javaux, I. Maksimovic, V. Loriette, B. Dubertret, *ACS Nano* **2012**, *6*, 6751.
[48] T. Váczi, *J. Appl. Spectrosc.* **2014**, *68*, 1274.
[49] J. Lee, T. W. Saucer, A. J. Martin, D. Tien, J. M. Millunchick, V. Sih, *Nano Lett.* **2011**, *11*, 1040.
[50] C. T. Le, D. J. Clark, F. Ullah, J. I. Jang, V. Senthilkumar, Y. Sim, M.-J. Seong, K.-H. Chung, J. W. Kim, S. J. A. P. Park, *ACS Photonics* **2017**, *4*, 38.
[51] S. Oswald, R. Reiche, *Appl. Surf. Sci.* **2001**, *179*, 307.
[52] L. Ren, H. Zhang, P. Tan, Y. Chen, Z. Zhang, Y. Chang, J. Xu, F. Yang, D. Yu, *J. Phys. Chem. B* **2004**, *108*, 4627.
[53] C. Xing, Z. Xie, Z. Liang, W. Liang, T. Fan, J. S. Ponraj, S. C. Dhanabalan, D. Fan, H. Zhang, *Adv. Opt. Mater.* **2017**, *5*, 1700884.
[54] C. Bousige, F. Balima, D. Machon, G. Pinheiro, A. Torres-Dias, J. Nicolle, D. Kalita, N. Bendiab, L. Marty, V. Bouchiat, *Nano Lett.* **2017**, *17*, 21.
[55] L. Properzi, A. Polian, P. Munsch, A. Di Cicco, *High Pressure Res.* **2013**, *33*, 35.
[56] G. Lucovsky, A. Mooradian, W. Taylor, G. Wright, R. Keezer, *Solid State Commun.* **1967**, *5*, 113.
[57] N. Hussain, Y. Yisen, R. U. R. Sagar, T. Anwar, M. Murtaza, K. Huang, K. Shehzad, H. Wu, Z. Wang, *Nano Energy* **2021**, *83*, 105790.
[58] G. Kresse, J. Furthmüller, *Phys. Rev. B* **1996**, *54*, 11169.
[59] J. P. Perdew, K. Burke, M. Ernzerhof, *Phys. Rev. Lett.* **1996**, *77*, 3865.
[60] A. Savin, R. Nesper, S. Wengert, T. F. Fässler, *Angew. Chem., Int. Ed.* **1997**, *36*, 1808.